Ground-state and transition charge densities in ^{192}Os

W. Reuter,* E. B. Shera, and M. V. Hoehn
Los Alamos National Laboratory, Los Alamos, New Mexico 87545

F. W. Hersman and T. Milliman
Department of Physics, University of New Hampshire, Durham, New Hampshire 03824

J. M. Finn, C. Hyde-Wright, R. Lourie, B. Pugh, and W. Bertozzi
Department of Physics and Laboratory for Nuclear Science, Massachusetts Institute of Technology, Cambridge, Massachusetts 02139
(Received 9 May 1984)

Elastic and inelastic electron-scattering cross sections of an Os-Pt transition region nucleus, ^{192}Os, have been measured in a momentum transfer range from 0.6 to 2.9 fm^{-1}. The data for the ground and the $J^\pi=2^+$, $2^{+\prime}$, 4^+, and 3^- states were analyzed model independently with a Fourier-Bessel parametrization of the ground state and transition charge densities. The normalization of the (e,e′) cross sections was obtained from a combined analysis with muonic-atom data for the ground and first 2^+ states. The densities and their radial moments are compared with theoretical predictions of the Davydov model and with axially symmetric deformed density-matrix-expansion Hartree-Fock calculations (including the Legendre expansion and the small-amplitude vibration model extensions).

I. INTRODUCTION

The osmium and platinum nuclei, lying in a region where the nuclear shape changes from prolate to oblate, provide a crucial testing ground for nuclear structure models that attempt to describe collective degrees of freedom. This shape transition, which is manifest experimentally by, for example, a change in sign of the quadrupole moment of the first 2^+ state, was predicted more than a decade ago by the pairing-plus-quadrupole (PPQ) model of Kumar and Baranger.[1] Over the years, the shape transition and the prospect of γ instability in the transitional nuclei have motivated much experimental and theoretical work.[2–6] Of particular current interest are the boson calculational methods: the interacting boson approximation (IBA) of Arima and Iachello[7] and the boson expansion theory (BET) of Kishimoto and Tamura,[8] which are quite successful at describing energy spectra and γ-ray branching ratios in the osmium and platinum nuclei.

The Hartree-Fock method is a well-established technique for describing ground states of nuclei, but its application to the transitional nuclei has not so far been thoroughly explored. For example, recently developed Hartree-Fock codes,[9,10] based on the density matrix expansion (DME) effective Hamiltonian, have been shown to accurately describe the charge radii of well-deformed nuclei. However, the extension of these calculations to transitional nuclei has not yet been attempted.

Experimentally, transition nuclei have been explored primarily in terms of integral quantities such as transition rates, electric and magnetic moments, reaction cross sections, and energy level spectra. Geometric information, such as the shape or radial behavior of the nuclear density, is blurred or entirely missing in these observables. However, advances in the technology of high-resolution electron scattering now make it possible to determine, accurately and model independently, the spatial distribution of electromagnetic densities in heavy deformed and transitional nuclei.

The present work, together with our Letter (Ref. 11), is the first report of an electron-scattering experiment on a nucleus in the osmium-platinum transition region. ^{192}Os was chosen for this study because it lies at the prolate-oblate transition that seems to occur between ^{192}Os and ^{194}Pt, and may thus most strongly show features characteristic of transitional nuclei.

II. ELECTRON SCATTERING ANALYSIS

In the plane-wave Born approximation, the electron-scattering cross section is given by[12]

$$\frac{d\sigma}{d\Omega}=\sigma_M\left\{\sum_{\lambda\geq 0}|F_\lambda^C(q)|^2+[\tfrac{1}{2}+\tan^2(\theta/2)]\sum_{\lambda\geq 1}[\,|F_\lambda^E(q)|^2+|F_\lambda^M(q)|^2]\right\}, \tag{1}$$

where σ_M, the Mott cross section, is given by

$$\sigma_M=(Z\alpha/2E)^2\cos^2(\theta/2)/[\eta\sin^4(\theta/2)]\,, \tag{2}$$

and η, the recoil factor, by

$$\eta=[1+(2E/M)\sin^2(\theta/2)]^{-1}\,. \tag{3}$$

In Eq. (1), Z is the atomic number of the target nucleus, α is the fine-structure constant, E is the incident electron energy, θ is the scattering angle, and M is the mass of the target nucleus. The momentum transfer q is approximated by

$$q \sim 2E\eta^{1/2}(1-\omega/E_0)^{1/2}\sin(\theta/2) , \quad (4)$$

where ω is the energy to which the nucleus is excited.

Only the longitudinal and the transverse electric form factors contribute to the excitation of the natural parity states studied in this work. These form factors are related to the nuclear one-body transition densities via a Fourier-Bessel transformation[13] that yields for the longitudinal form factor

$$F_\lambda^C(q)=\frac{J_f}{J_i}\int \rho_\lambda(r) j_\lambda(qr) r^2 dr . \quad (5)$$

The nuclear current densities $J_{\lambda,\lambda+1}$ and $J_{\lambda,\lambda-1}$ are related to the transverse electric form factor via Eq. (6) in Ref. 13. Since the dynamics of collective motion behave like irrotational and incompressible flow,[14] the divergenceless current $J_{\lambda,\lambda+1}$ can be neglected. Therefore, the remaining current term $J_{\lambda,\lambda-1}$, which is called the irrotational and incompressible current, is uniquely tied to the transition charge density $\rho_\lambda(r)$ through the continuity equation. Since we discuss only collective states, this method is suitable for extracting the transition charge densities.

The description of electron scattering based on the plane-wave Born approximation does not include the distortion of the electron waves by the Coulomb field of the nucleus. In contrast, a description based on the distorted-wave Born approximation (DWBA), which treats the electron-nucleus interaction in lowest order perturbation theory, yields electron waves that are solutions of the Dirac equation in the presence of the spherically symmetric part of the ground-state charge distribution. To first order, distortion of the electron waves increases the momentum transfer that characterizes the scattering event. The relation between the momentum transfer q, as calculated from the kinematics of the scattering process, and the effective momentum transfer $q_{\rm eff}$, which characterizes the wavelength of the probe in the vicinity of the nucleus, is given by

$$q_{\rm eff}=q\left[1+\tfrac{3}{2}\sqrt{(3/5)}\frac{Ze^2}{E\langle r^2\rangle^{1/2}}\right] , \quad (6)$$

where $\langle r^2\rangle^{1/2}$ is the rms radius of the nuclear charge distribution.

In this experiment, all of the analysis was carried out with the DWBA method.

III. EXPERIMENTAL DETAILS

The experiment was performed at the electron-scattering facility of the MIT-Bates Accelerator Laboratory. The accelerator and the high-resolution energy-loss spectrometer system have been described elsewhere.[15,16] However, the detector system has been improved recently and a short description of the modification is in order. As originally constructed, the detector system consisted of a single vertical drift chamber (VDC), positioned close to the focal plane of the spectrometer, and two multiwire proportional counters (transverse arrays), located behind the VDC. The sense wires of the VDC and of the transverse arrays are parallel and perpendicular, respectively, to the lines of constant momentum on the spectrometer focal plane. Two Čerenkov counters (located behind the wire chambers) provide an event trigger and a fiducial starting time for the delay-line readout of the chamber. This detector system has been modified by adding a second VDC (located 6 cm behind the first VDC) that provides a second position measurement for the electron track and thus allows a much more accurate determination of the vertical angle of the incoming electron. This greater accuracy eliminates certain types of spectrum nonuniformities.[17] Information from the second VDC also improves the system resolution and peak line shape through more precise aberration corrections.

Two ^{192}Os targets with osmium thicknesses of 8.9 and 22.3 mg/cm^2 were fabricated for use in the experiment. These targets, enriched to 99.07%, consisted of a centrifugally deposited and sintered osmium layer sandwiched between two 12.6 mg/cm^2 carbon foils.[18] Because the fabrication procedure involved the use of an organic binder [polyvinyl alcohol, $(CH_2CHOH)_x$], the targets contained an oxygen impurity to the extent of about 0.1 mg/cm^2. Impurities in the carbon foils were also detected in the scattering spectra and consisted of about 0.08 mg/cm^2 ^{28}Si and smaller amounts of ^{14}N and ^{32}S. The target thicknesses were determined by normalizing the elastic cross sections with muonic-atom data according to the procedure discussed in Sec. IV A.

The spectrometer was operated in the dispersed beam (energy-loss) mode to achieve high resolution and simultaneously high beam intensity on the target (in this experiment, up to 30 μA). We used incident electron energies of 150, 250, 355, and 364 MeV; at each energy the scattering angle was varied between 42° and 98° in increments of 5°–8°. This method of changing the momentum transfer was preferable to constantly changing the incident energy (which requires retuning the dispersion matching magnets to optimize the spectrometer resolution), since a sliding-seal target chamber arrangement made it possible to change the spectrometer angle in less than 30 min. The scattering angles were chosen at each energy so that in most cases the impurity peaks were kinematically separated from the ^{192}Os levels. This procedure provides, at the different incident energies, data points that overlap in q space, and thus a check of systematic uncertainties in scattering angle and incident energy. In total, a momentum transfer region of $0.6 \le q \le 2.9$ fm^{-1} was covered. The spectrum resolution, although dominated by the thickness of our targets (34 and 48 mg/cm^2, including the carbon foil), was less than 60 keV even at the highest incident beam energy. This resolution was sufficient to separate the $2^{+'}$ and 4^+ levels in ^{192}Os, which differ in energy by 91 keV.

The incident electron energies and the linear and quadratic dispersion parameters of the spectrometer were obtained by measuring the focal plane positions of the elastic and inelastic peaks of ^{9}Be, ^{16}O, and ^{27}Al. The incident electron energy was computed, with an uncertainty always less than 0.2%, by comparing the recoil energies of the lighter isotopes with the well-known excitation energies of the heavier isotopes.

A total of 28 spectra were taken to determine the angular distributions of the (e,e') cross sections for the ground

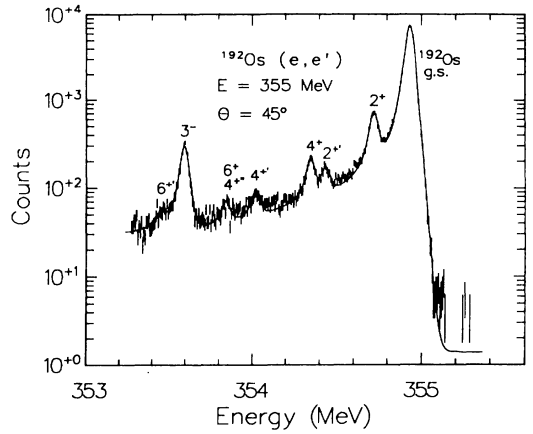

FIG. 1. Spectrum of scattered electrons with incident energy 355 MeV and scattering angle 45° from ^{192}Os.

and low-lying inelastic states of ^{192}Os. The ratio of the thicknesses of the two targets was determined from the ratio of the elastic cross sections measured at the same scattering angle. Separate normalization runs were also made at each energy and angle using a standard carbon-foil target of known thickness. Figure 1 is a typical osmium spectrum, measured at 355 MeV and a scattering angle of 45°. The clear separation of the $2^{+'}$ and 4^{+} states of ^{192}Os is even more pronounced at lower incident energies.

IV. DATA REDUCTION AND ERROR ANALYSIS

We extracted the elastic and inelastic electron-scattering cross sections by using the MIT line-shape fitting program ALLFIT, in which an asymmetric hyper-Gaussian shape is folded with the spectral components produced by Landau straggling, bremsstrahlung, and Schwinger radiation.[19] With the exception of the width parameters, the same line-shape parameters were used for osmium, carbon, and the impurity lines. A different width parameter was fitted for the lighter elements to account for the different kinematic broadening effect caused by the finite solid angle. In general, the excitation energies of the fitted inelastic levels or the centroids of the impurities (all elastic) were allowed to vary only when the peaks were well defined and resolved. Otherwise, they were locked to the known excitation energies or fixed according to kinematics relative to the elastic osmium peak. For the spectra at low momentum transfer, it was sufficient to adjust a constant background. In the higher-q range the spectra contained a background that increased slowly with increasing excitation energy, and subtraction of a linear (or mildly quadratic) background was required.

The carbon elastic peak from the carbon foils of our sandwich target provided a very useful internal cross-section normalization for each spectrum. Since this normalization was independent of spectrometer solid angle, chamber dead-time corrections, and charge normalization of the incoming beam, it was used in preference to the separate standard carbon foil normalization. The elastic carbon cross sections used in the normalization were taken from a recent electron-scattering experiment at Mainz.[20] This method of extracting relative cross sections relies, of course, on the constancy of the detector efficiency across the focal plane, since the carbon peak changes location by an amount that depends upon the difference in recoil energies between carbon and osmium at each energy and angle. The variation in focal plane efficiency was checked[13] by measuring the elastic peak of ^{208}Pb at several locations along the focal plane and was found to be less than 1.5%. Dead time effects were assumed to be uniform across the focal plane for peaks with different counting rates. This assumption has been tested[21] by measuring a ^{16}O spectrum twice, once at a low counting rate and once at a high rate. From each spectrum, the ratio of the cross sections for the ground and first excited states (1.98 MeV) of oxygen was extracted. The two agreed within statistical limits ($<1\%$).

The statistical uncertainty of the experimental cross section of each peak was determined in a conservative fashion by taking the larger of (a) the square root of the number of counts assigned to the peak, or (b) the correlated fitting error calculated by adding in quadrature the changes in the area generated by increasing each fit parameter by its estimated uncertainty. The statistical uncertainties were then multiplied by the square root of χ^2 per degree of freedom that resulted from the line fitting procedure, which usually lies between 0.8 and 2. The errors for the osmium cross sections were computed by adding quadratically the uncertainties in the osmium and carbon areas.

Investigation of the homogeneity of our osmium target by means of elastic proton scattering[18] revealed local target thickness variations of 7%. Since the dispersed beam of the Bates accelerator covers a relatively large area ($\sim$0.5 by 2.0 cm) of the target, these inhomogeneities are largely averaged out. Nevertheless, to include uncertainties due to positional instability of the beam spot on the target and due to possible minor changes in the local efficiency of the detector system along the focal plane, an additional error of 2% was added quadratically to the cross sections. The elastic and inelastic electron-scattering cross sections for ^{192}Os are listed in Table I.

Compared with the data discussed in our earlier Letter[11] (which concerned only the ground and first excited states of ^{192}Os), the present data set contains a few additional points at low q and additional points at high q that extend the q range up to 2.9 fm^{-1}.

V. ANALYSIS OF THE CROSS SECTIONS

A. Elastic cross sections

1. Fourier-Bessel method

Among the various methods for determining the nuclear charge distribution from the measured cross sections, we used the one introduced by Dreher *et al.*[22] This method involves expanding the nuclear charge distribution into a Fourier-Bessel series,

TABLE I. Elastic and inelastic electron scattering cross sections for ^{192}Os. All cross sections are normalized relative to the carbon data of Ref. 20. The absolute normalizations for the ground state and the first 2^+ state were obtained by including the muonic data in the analysis. The normalization for the higher states was taken from the renormalized elastic cross sections. All listed data are corrected for finite solid angle and multiple scattering. The quoted errors are discussed in Sec. IV.

Energy (MeV)	θ (deg)	0^+ ground state (mb)	2^+ 206 keV (mb)	$2^{+\prime}$ 489 keV (mb)	4^+ 580 keV (mb)	3^- 1341 keV (mb)
149.70	42.0	$0.3456(78)\times10^{+1}$	$0.1231(46)\times10^{+0}$			$0.117(27)\times10^{-1}$
	47.0	$0.1336(27)\times10^{+1}$	$0.5598(169)\times10^{-1}$	$0.423(68)\times10^{-2}$		$0.691(65)\times10^{-2}$
	52.0	$0.6412(129)\times10^{+0}$	$0.2087(57)\times10^{-1}$	$0.174(19)\times10^{-2}$	$0.152(21)\times10^{-2}$	$0.439(31)\times10^{-2}$
	52.0	$0.6497(133)\times10^{+0}$	$0.2048(86)\times10^{-1}$	$0.177(35)\times10^{-2}$		$0.436(55)\times10^{-2}$
	58.0	$0.3192(65)\times10^{+0}$	$0.6231(207)\times10^{-2}$	$0.517(87)\times10^{-3}$	$0.137(9)\times10^{-2}$	$0.169(19)\times10^{-2}$
	59.0	$0.2891(59)\times10^{+0}$	$0.5250(187)\times10^{-2}$		$0.150(16)\times10^{-2}$	$0.147(32)\times10^{-2}$
	64.0	$0.1461(30)\times10^{+0}$	$0.2863(103)\times10^{-2}$	$0.350(76)\times10^{-3}$	$0.951(80)\times10^{-3}$	$0.599(157)\times10^{-3}$
	66.0	$0.1130(24)\times10^{+0}$	$0.2272(144)\times10^{-2}$	$0.264(83)\times10^{-3}$	$0.916(91)\times10^{-3}$	
	74.0	$0.2789(61)\times10^{-1}$	$0.1821(81)\times10^{-2}$	$0.214(25)\times10^{-3}$	$0.390(28)\times10^{-3}$	
	78.0	$0.1280(27)\times10^{-1}$	$0.1628(41)\times10^{-2}$			
	82.0	$0.5923(129)\times10^{-2}$	$0.1161(52)\times10^{-2}$	$0.135(7)\times10^{-3}$	$0.148(8)\times10^{-3}$	$0.471(72)\times10^{-4}$
	84.0	$0.4257(93)\times10^{-2}$	$0.9814(263)\times10^{-3}$	$0.123(8)\times10^{-3}$		$0.424(45)\times10^{-4}$
	90.0	$0.2405(50)\times10^{-2}$	$0.5087(185)\times10^{-3}$	$0.624(30)\times10^{-4}$	$0.373(26)\times10^{-4}$	
	98.0		$0.1453(52)\times10^{-3}$	$0.165(14)\times10^{-4}$	$0.795(122)\times10^{-5}$	$0.399(15)\times10^{-4}$
248.00	44.0	$0.9171(208)\times10^{-1}$	$0.5486(241)\times10^{-2}$	$0.684(139)\times10^{-3}$		
	56.0	$0.5318(116)\times10^{-2}$	$0.7515(279)\times10^{-3}$	$0.912(88)\times10^{-4}$	$0.568(83)\times10^{-4}$	$0.143(11)\times10^{-3}$
	64.0	$0.2033(43)\times10^{-2}$	$0.1036(57)\times10^{-3}$	$0.117(28)\times10^{-4}$	$0.242(20)\times10^{-4}$	$0.581(29)\times10^{-4}$
	70.0	$0.4366(98)\times10^{-3}$	$0.1148(38)\times10^{-3}$	$0.117(10)\times10^{-4}$	$0.246(13)\times10^{-4}$	$0.171(10)\times10^{-4}$
	76.0	$0.8164(214)\times10^{-4}$	$0.6827(247)\times10^{-4}$	$0.936(57)\times10^{-5}$	$0.102(6)\times10^{-4}$	$0.262(31)\times10^{-5}$
	84.0	$0.6583(175)\times10^{-4}$	$0.1189(54)\times10^{-4}$	$0.197(19)\times10^{-5}$	$0.133(17)\times10^{-5}$	$0.229(19)\times10^{-5}$
	90.0	$0.3273(124)\times10^{-4}$	$0.2532(191)\times10^{-5}$	$0.279(78)\times10^{-6}$	$0.280(76)\times10^{-6}$	$0.146(12)\times10^{-5}$
355.00	45.0	$0.3335(75)\times10^{-2}$	$0.2104(81)\times10^{-3}$			
	88.0	$0.796(239)\times10^{-7}$	$0.1144(236)\times10^{-6}$			
	98.0	$0.220(220)\times10^{-8}$				
364.00	45.0	$0.2408(87)\times10^{-2}$	$0.2469(106)\times10^{-3}$	$0.271(22)\times10^{-4}$	$0.602(31)\times10^{-4}$	$0.877(25)\times10^{-4}$
	66.0	$0.5381(236)\times10^{-5}$	$0.7805(316)\times10^{-5}$	$0.856(86)\times10^{-6}$	$0.149(10)\times10^{-5}$	$0.647(61)\times10^{-6}$
	72.0	$0.2527(121)\times10^{-5}$	$0.2215(107)\times10^{-5}$	$0.290(40)\times10^{-6}$	$0.575(51)\times10^{-6}$	$0.113(24)\times10^{-6}$
	78.0	$0.9147(384)\times10^{-6}$	$0.2180(197)\times10^{-6}$	$0.507(106)\times10^{-7}$	$0.346(96)\times10^{-7}$	$0.714(99)\times10^{-7}$

$$\rho(r)=\sum a_n j_0(q_n r), \quad \text{for } r<R$$
$$=0, \quad \text{for } r\geq R\ , \tag{7}$$

where the cutoff radius R is taken to be well outside the nuclear volume. The values q_nR give the nth zero of the spherical Bessel function, so that $j_0(q_nR)=0$ with $q_n=n\pi/R$. Only coefficients a_n with $n\leq Rq_{max}/\pi$ are well determined by an experiment that measures the cross sections up to a momentum transfer q_{max}. Lack of data at higher momentum transfer causes the so-called incompleteness error[22] that limits our knowledge of the charge distribution primarily in the nuclear interior. The incompleteness error was calculated by using an asymptotic estimate[22] of an upper limit for the form factor at $q>q_{max}$, namely,

$$|F(q)|\leq c\cdot q^{-4}\cdot F_p(q)\ , \tag{8}$$

where $F_p(q)=\exp(-q^2\langle r^2\rangle_p/6)$ is the proton form factor, and the proton radius $\langle r^2\rangle_p$ was taken to be 0.86 fm.[20] Twelve Fourier-Bessel coefficients were fitted, and the maximum q_n was extended to about 3.5 fm^{-1}. The constant c was computed by matching the envelope of $F(q)$ at the last measured maximum of the form factor.

The Fourier-Bessel method yields the charge distribution, including its error band, and has the advantage that the statistical and completeness errors, which contribute to this band, can be easily distinguished.

2. *Muonic normalization (elastic)*

Muonic-atom data provide a precise and model-independent moment of the monopole charge distribution, the so-called Barrett moment,[23,24] defined by

$$\langle r^k e^{-\alpha r}\rangle=\frac{1}{Z}\int \rho(r) r^k e^{-\alpha r} 4\pi r^2 dr\ . \tag{9}$$

As pointed out in Ref. 24, the Barret moments are very useful in normalizing electron-scattering cross sections, and substantially reduce the errors of the radial moments in a combined analysis. The largest uncertainty in the normalization of the osmium cross sections stems from the target thickness, which was difficult to determine absolutely because of the method used to fabricate the target. Therefore we performed a combined analysis of the electron-scattering data with the muonic data of Ref. 25 (see Table II) and adjusted the normalization of the electron-scattering data. The two sets of data from the two targets were adjusted to each other by using the experimentally determined ratio of the thicknesses of the two targets.

3. *Cutoff radius, errors, and ground-state results*

Some model dependence is introduced by the choice of the cutoff radius R. Therefore we made fits with various values of R between 10 and 12 fm and found that χ^2 did not significantly improve for $R>11$ fm. Similarly, extracted values of the rms radius and the normalization parameter for the (e,e') data did not charge significantly for $R>11$ fm, nor did the charge distribution show any significant change. Consequently, the cutoff radius was chosen to be 11 fm. The experimental cross sections (recalculated for an energy of 364 MeV) and the Fourier-Bessel fit are shown in Fig. 2. The corresponding charge distribution is shown in Fig. 3, and the rms radius is listed in Table III.

TABLE II. Muonic atom parameters (Ref. 25) used in the combined analysis of the ground state and first excited state electron scattering data.

	Ground state	2^+ state
A (fm^{-3})		-0.87152×10^{-3}
B (fm^{-m-3})		0.10047×10^{-4}
k	2.3065	
m		2.3790
α (fm^{-1})	0.1445	0.1477
B (fm^k)	21.283(9)[a]	
W (fm^{-1})		0.07311(32)[b]

[a]Statistical error (0.02%) plus contribution from nuclear polarization (0.04%).
[b]Total error with the following contributions (see Ref. 27): statistical (0.37%), charge model (0.06%), $M1$ distribution (0.2%), and nuclear polarization (0.1%). All errors are added in quadrature.

We conclude from the small χ^2 of the fit (see Table III) and from the excellent agreement between experimental and fitted data (see Fig. 2) that the data taken at different energies and angles are consistent and show no energy- or angle-related systematic errors. In our analysis, oscillations leading to negative charge densities at large radii have been suppressed.[14,11] However, we also performed fits without this constraint and found no indication of oscillations. This fact again implies the absence of signifi-

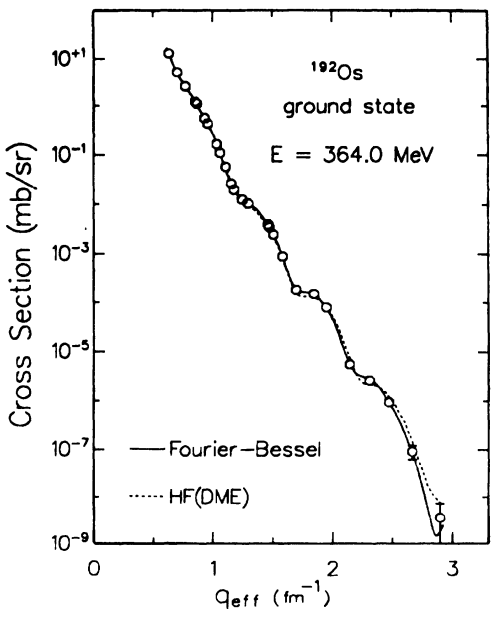

FIG. 2. Experimental elastic electron-scattering cross sections (recalculated for 364 MeV) of ^{192}Os. The cross sections are compared with the Fourier-Bessel fit and the Hartree-Fock calculation. Errors smaller than the circle diameter are not drawn.

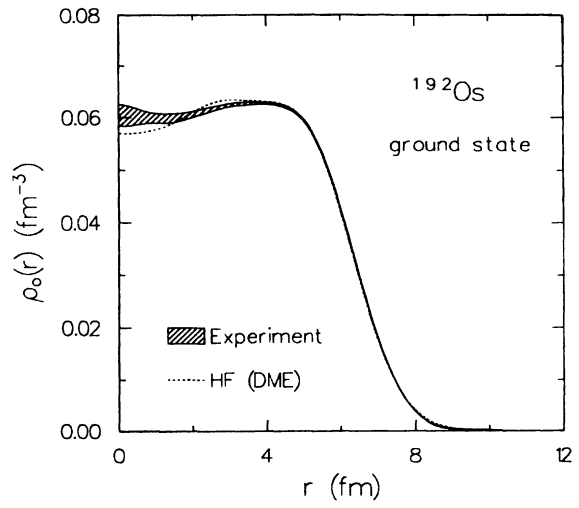

FIG. 3. Experimental and Hartree-Fock ground state charge density for ^{192}Os. The error band shown includes statistical and completeness errors. The normalization of the charge distribution is given as $\int \rho(r)r^2dr = Z/4\pi$.

cant systematic errors in the cross sections, particularly in the normalization, which can readily cause a negative lobe in the tail of the charge distribution.[26]

The Fourier-Bessel coefficients and their statistical errors are given in Table IV. The dominant contribution to the error band of the charge distribution arises from the statistical uncertainties of the cross sections. Only in the interior of the nucleus, where the total error is largest, does the incompleteness error exceed the statistical uncertainty (by about 20%). Increasing the number of Fourier-Bessel coefficients to 15 enlarged the incompleteness error at $r=0$ by only a few percent and did not have any significant effect on the shape of the charge density or the χ^2 value. Therefore, 12 coefficients were considered sufficient to fit the present data.

The combined analysis yields a relatively small error in the rms radius. The statistical component of this error amounts to 0.003 fm, and a contribution of 0.001 fm was derived from the variation of the rms radius with a change of R from 11 to 12 fm. Systematic uncertainties in the carbon cross sections were taken from Ref. 20; this uncertainty produces an error in the ^{192}Os rms radius of 0.001 fm. Quadratic addition of all contributions leads to the total error listed in Table III. The same considerations (but without the systematic contribution) were used to determine the total error of the normalization parameter for the (e,e') data, which also can be found in Table III.

B. Inelastic cross sections

1. Fourier-Bessel method

The inelastic data were analyzed following the method of Heisenberg.[14] In this approach, the transition density $\rho_\lambda(r)$, from the ground state to an excited state, is described by

$$\rho_\lambda(r)=\sum a_n q_n^{\lambda-1} j_\lambda(q_n^{\lambda-1}r), \quad \text{for } r<R$$
$$=0, \quad \text{for } r\geq R\ , \tag{10}$$

where R is the transition density cutoff radius. The values $q_n^{\lambda-1}R$ are the nth zeros of the spherical Bessel function of order $\lambda-1$. The constraint that the transition density must vanish at the cutoff radius R imposes a condition on the coefficients a_n. We estimated the incompleteness error, in a manner similar to that used for the elastic cross sections, by generating pseudodata beyond $q_{\max}$ with an upper limit for the squared form factor of $c\sim\exp(-\alpha q)$. The parameters c and α were chosen to give a reasonable envelope at $q<q_{\max}$. The data for all inelastic levels were fitted by adjusting 12 Fourier-Bessel coefficients. The transition probability and transition radius are defined as

$$\sqrt{B(E\lambda:0^+\rightarrow\lambda)}=\sqrt{(2\lambda+1)}\int\rho_\lambda(r)r^{\lambda+2}dr \tag{11}$$

and

$$R_{\rm tr}^2=\int\rho_\lambda(r)r^{\lambda+4}dr\Big/\int\rho_\lambda(r)r^{\lambda+2}dr\ . \tag{12}$$

Use of the Fourier-Bessel expansion may introduce oscillations in the extracted density at large radii because of the limited q range over which the cross sections are determined. Therefore, the method of constraining the tail of the transition density by an exponential function[14] was applied.

TABLE III. Experimental results for ground and excited states of ^{192}Os from Fourier-Bessel analysis.

λ^π	No. of points	χ^2	$\langle r^2\rangle^{1/2}$ or $R_{\rm tr}$ (fm)	$B(E\lambda:0^+\rightarrow\lambda)$ (e^2b$^\lambda$)	Normalization factor
0^+	27	16.7	5.413(4)[a]		0.994(12)
2^+	27	23.9	6.950(61)[a]	2.009(32)	0.978(31)
$2^{+\prime}$	22	8.4	7.04(15)	0.189(32)	0.994[b]
4^+	19	15.5	6.894(79)	0.0365(42)	0.994[b]
3^-	20	15.3	7.18(33)	0.130(34)	0.994[b]

[a]Analysis includes muonic atom data.
[b]Normalization taken from 0^+ state.

TABLE IV. Fourier-Bessel coefficients a_n as defined in Sec. IV A and IV B for the ground and excited states of ^{192}Os. The errors represent the diagonal elements of the error matrix. A cutoff radius of 11 fm was used for all states, and for the transition charge distributions a tail constraint was applied. The coefficients a_n for the ground state charge distribution are normalized to $\int \rho(r) r^2 dr = 1$. The normalization for the coefficients a_n of all transition densities is given by Eq. (11).

n	0^+ ground state	2^+ 206 keV	$2^{+'}$ 489 keV	4^+ 580 keV	3^- 1341 keV
1	0.0097614(29)	0.029985(185)	0.009223(754)	0.005946(645)	0.008713(623)
2	0.0068609(393)	0.033852(1266)	0.009601(1450)	0.011360(1483)	0.012111(1232)
3	−0.0082500(1047)	−0.013297(265)	−0.005448(499)	0.003943(399)	−0.000885(304)
4	−0.0016837(787)	−0.013953(335)	−0.005327(597)	−0.004232(369)	−0.006789(534)
5	0.0048058(443)	0.011124(271)	0.003783(418)	−0.001499(159)	−0.000186(129)
6	−0.0009487(579)	0.003754(180)	0.001987(218)	0.002016(181)	0.002340(192)
7	−0.0015268(534)	−0.005344(160)	−0.001698(198)	0.000606(134)	−0.000142(104)
8	0.0005980(318)	−0.001160(230)	−0.000671(180)	−0.000464(326)	−0.000448(171)
9	0.0004751(757)	0.001208(321)	−0.000620(340)	−0.000233(421)	−0.000010(322)
10	0.0000400(742)	0.000587(818)	−0.000624(308)	−0.000172(239)	0.000069(170)
11	−0.0002772(1947)	−0.000505(418)	0.000066(294)	−0.000020(196)	−0.000015(111)
12	0.0001217(1506)	−0.000337(222)	0.000206(164)	0.000081(117)	−0.000012(54)

2. *Muonic normalization (inelastic)*

As pointed out in Ref. 27, it is possible to perform a simultaneous analysis of inelastic electron-scattering and muonic atom hyperfine-splitting (HFS) data. Inclusion of the muonic HFS data considerably improves the accuracy of the normalization for the inelastic (e,e') data[27] and, with it, the accuracy of the extracted $B(E2)$ values. The method is particularly applicable to deformed nuclei with low-lying excited states that connect to the ground state by strong $E2$ transitions. In such cases the strong quadrupole interaction between the muonic $2p$ levels and the low-lying nuclear states leads to a hyperfine splitting of the muonic states that can typically be measured with an uncertainty of less than 0.5%. The observed HFS energies are directly related[27] to the model-independent quantity $W^{I'j'Ij}$ by

$$W^{I'j'Ij} = \int \rho_{\rm tr}^{I'I}(r) V_\mu^{j'j}(r) r^2 dr \ . \tag{13}$$

Here, $\rho_{\rm tr}^{I'I}(r)$ is the transition density between nuclear states $|I\rangle$ and $|I'\rangle$, and $V_\mu^{j'j}(r)$ is the muon-generated potential between muon states j and j'. The muon potential can be approximated[31] by an analytic function of the form

$$V_\mu^{j'j}(r) = r^\lambda [A + Br^m \exp(-\alpha r)] \ , \tag{14}$$

where the parameters A, B, m, and α are determined from a least-squares fit to the numerically computed muon potential. In the case of osmium, this combined analysis was applied to the first 2^+ state for which a precise value of W is available from the muonic work of Ref. 25. The transition density constraint that we used in fitting the (e,e') data is then

$$W = \sqrt{(2\lambda+1)} \int \rho_2(r)(A + Br^m e^{-\alpha r}) r^{\lambda+2} dr \ . \tag{15}$$

This procedure allows an independent normalization of the inelastic electron-scattering cross sections, which can be compared to (and should agree with) that derived from the elastic combined analysis.

3. *The 2^+ state*

Because of its comparatively large cross section, the first 2^+ state (206 keV) provides, among all excited states, inelastic data of the highest statistical accuracy. Analysis of this data is also favored by the existence of precise muonic-atom normalization data[25] that permits us to use the inelastic combined analysis method discussed in the preceding section. For the calculations we used a modified version of the DWBA code of Heisenberg[14,28] and the muonic constraint parameters listed in Table II. We investigated in detail the influence of variations of the cutoff radius R and the matching radius R_1 for the tail constraint[27] on the normalization of the (e,e') data and the extracted $B(E2)$ value. R values between 10 and 12 fm were found to produce a nearly constant χ^2 value of about 24 (for 27 data points). Values of R_1 (the radius where the tail constraint begins) between 9 and 9.5 fm were found to be appropriate and produced results in good agreement with those obtained with no tail constraint.

The excellent agreement between the experimental cross sections and the Fourier-Bessel fit is demonstrated in Fig. 4. The extracted transition charge density is displayed in Fig. 5, and the corresponding Fourier-Bessel coefficients are listed in Table IV.

As expected in view of the high collectivity of the 2^+ state (about 61 W.u.), the transition density exhibits a strong peak at the surface of the nucleus. The interior structure of the transition density is similar to that observed for the 2^+ rotational state of ^{154}Gd (Ref. 17) and of ^{152}Sm (Ref. 29). The error band of the 2^+ state, like that for the ground state density, is primarily determined at the nuclear surface by the statistical accuracy of the data and in the nuclear interior by the incompleteness error.

Values obtained for the transition probability $B(E2)$, the transition radius $R_{\rm tr}$, and the (e,e') normalization parameter vary slightly depending upon the cutoff radius chosen. We have therefore adopted values (see Table III) that represent averages over the realistic range of values of R and R_1. The quoted total error (see Table III) for

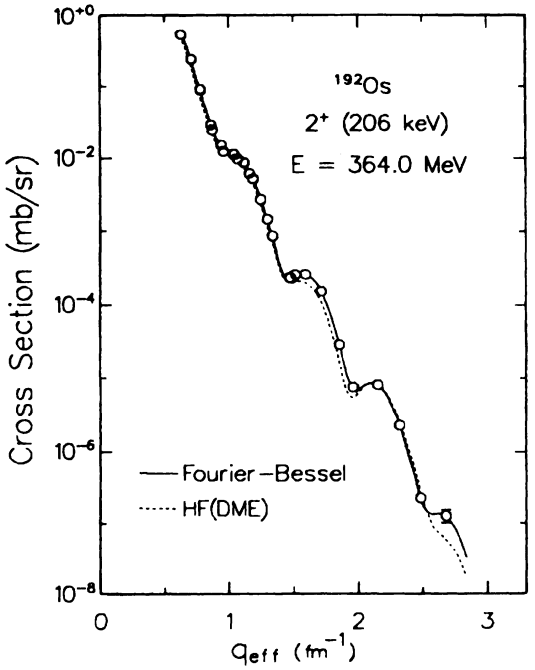

FIG. 4. Experimental inelastic electron-scattering cross sections (recalculated for 364 MeV) for the first 2^+ state (206 keV) of ^{192}Os. The data are compared with the Fourier-Bessel fit and the Hartree-Fock calculation.

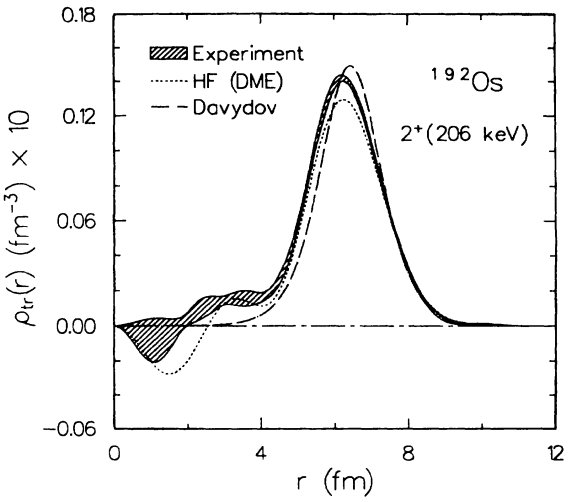

FIG. 5. Experimental transition charge density for the first 2^+ state (206 keV) of ^{192}Os. The error band shown includes statistical and completeness errors. The experimental transition density is compared with two theoretical predictions. The HF density is calculated using the Legendre expansion of the HF intrinsic charge distribution.

the $B(E2)$ contains the following contributions: uncertainty in the muonic moment W and statistical error in the electron-scattering data (1.3%), systematic errors including uncertainties in the reference cross sections (0.3%), and a systematic error (1.0%) representing the largest deviation observed in the $B(E2)$ as R and R_1 were varied over reasonable ranges.

The ratio of the elastic normalization to that of the 2^+ state inelastic normalization for our electron-scattering data was found to be 1.016±0.033. This consistency of the two independent normalizations represents an important test of the validity of both the muonic and (e,e') experiments, a topic discussed in detail in Ref. 27. The experimental $B(E2)$ value from our combined analysis is compared with Coulomb excitation results and theoretical predictions in Table V. The present result is seen to be in good agreement with the other experiments and is distinguished by its small uncertainty.

4. *The $2^{+'}$, 4^+, and 3^- states*

The inelastic data were of sufficiently good quality that we were able to use the Fourier-Bessel method to make model-independent determinations of the transition densities of the $2^{+'}$ (489-keV), 4^+ (580-keV), and 3^- (1341-

TABLE V. Comparison of the $B(E2)$ value and transition radius for the 2^+ (206 keV) state of ^{192}Os with other experiments and calculations.

$B(E2{:}0^+\rightarrow 2^+)$ (e^2b^2)	R_{tr} (fm)	Method	Ref.
2.009(32)	6.950(61)	(e,e')+μ	This work
2.123(50)		Coul. exc.	47
1.896		Coul. exc.	48
2.09(21)		Coul. exc.	49
1.99(11)		Coul. exc.	50
2.04(6)		Coul. exc.	51
2.22(34)		Coul. exc.	52
1.83	7.03	HF (DME)	This work
2.102		IBA	31
1.95		IBA	34
2.07		BET	35
2.58		PPQ	1
	7.06	Davydov+μ[a]	42

[a]Davydov transition density fitted to μ-atom data.

keV) states. Since muonic-atom data are not available for these states, normalization of the cross sections was taken from the elastic combined analysis. In other respects, the analysis procedure closely followed that used for the 2^+ state. For the $2^{+'}$ state, χ^2 converged to 8.4 (22 data points) for cutoff radii greater than 10 fm, and for the 4^+ state, χ^2 converged to 15.5 (19 data points) for R greater than 9 fm. The radial moments quoted in Table III were determined by averaging over reasonable R and R_1 regions.

The experimental cross sections together with the Fourier-Bessel fit are shown in Figs. 6 and 8. The corresponding transition densities are displayed in Figs. 7 and 9, and the Fourier-Bessel coefficients a_n are listed in Table IV. The error bands of the transition densities of the $2^{+'}$ and 4^+ states are relatively larger in the surface region of the nucleus because the large radiation tail of the elastic and first 2^+ states causes a larger uncertainty in the low-q inelastic cross sections.

The 4^+ state exhibits a transition density that peaks at a smaller radius than that of the first 2^+ level. This result differs from the results obtained for the deformed nuclei ^{154}Gd (Ref. 17) and ^{152}Sm (Ref. 30). This fact is consistent with the negative β_4 deformation of ^{192}Os as compared to the positive β_4 deformation of Gd and Sm. Calculations using a deformed Fermi model show that the difference in transition radii between the 2^+ and 4^+ states of these three nuclei is consistent in magnitude with that produced by the purely geometric effect of the different β_4 deformations in the three cases.

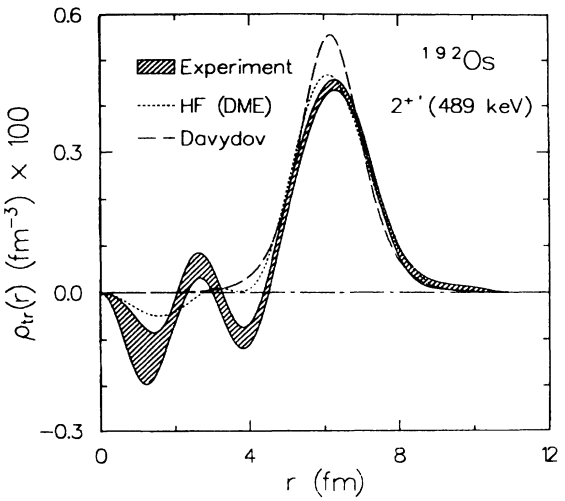

FIG. 7. Experimental transition charge density for the second 2^+ state (489 keV) of ^{192}Os. The error band shown includes statistical and completeness errors. The HF transition density is derived from the HF intrinsic density using the small amplitude vibration expansion.

The transition radius of the $2^{+'}$ state appears to be the same as or slightly larger than that of the lowest 2^+ state (see Table III). From a vibrational model viewpoint, we would expect the $2^{+'}$ γ band head to have a smaller transition radius than that of the 2^+ rotational band member. This expectation, which is based on the fact that the γ band is a shape oscillation involving the shorter of the two axes of the nuclear ellipsoid, is confirmed in ^{154}Gd (Refs. 17 and 43). The transition density for the $2^{+'}$ state of ^{192}Os also shows a more pronounced internal structure than the corresponding density in ^{154}Gd.

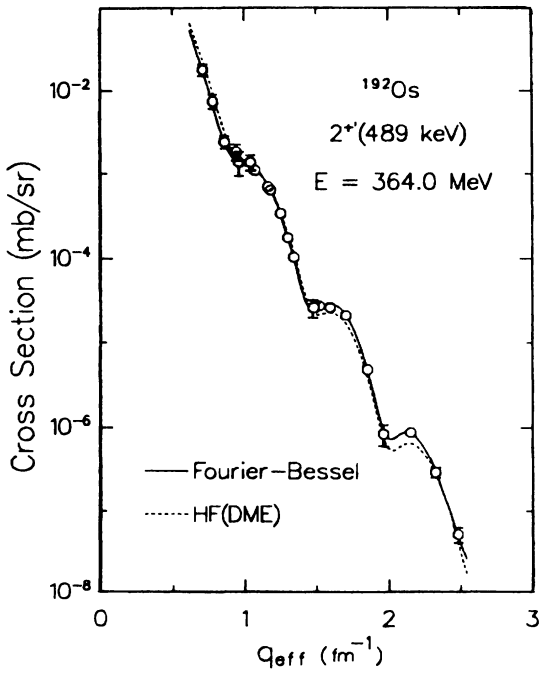

FIG. 6. Experimental inelastic electron-scattering cross sections (recalculated for 364 MeV) of the second 2^+ state (489 keV) of ^{192}Os. The data are compared with the Fourier-Bessel fit and the Hartree-Fock calculation.

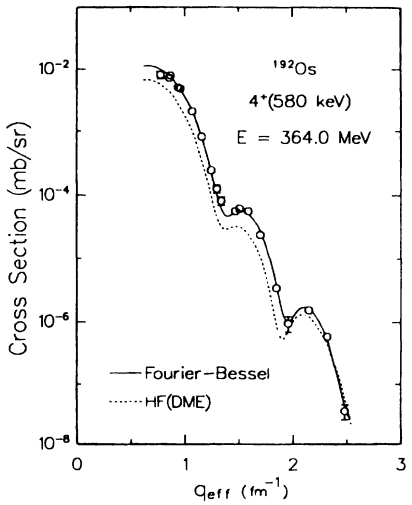

FIG. 8. Experimental inelastic electron-scattering cross sections (recalculated for 364 MeV) of the 4^+ state (580 keV) of ^{192}Os. The data are compared with the Fourier-Bessel fit and the Hartree-Fock calculation.

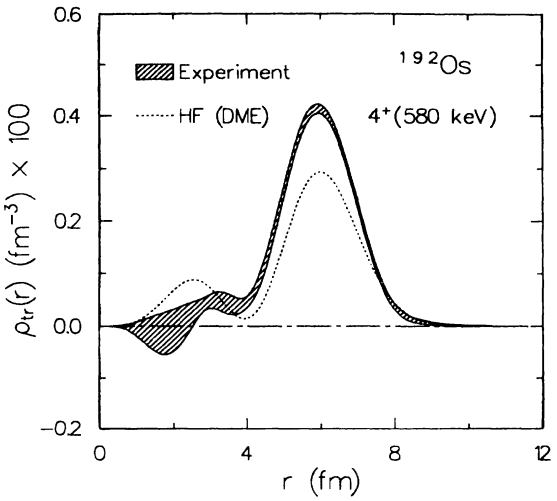

FIG. 9. Experimental transition charge density for the 4^+ state (580 keV) of ^{192}Os. The error band shown includes statistical and completeness errors. The Hartree-Fock density is calculated using the Legendre expansion of the HF intrinsic charge distribution.

Our experimental $B(E\lambda)$ values for the higher states are compared with other measurements and theories in Table VI. The $B(E2')$ value agrees well with Coulomb excitation measurements and with the IBA calculation from Ref. 31. In contrast to the only previous measurement of the $B(E4)$ value for the 4^+ state (580 keV), the present value is in reasonable agreement with the IBA calculation[31] and the prediction of Ref. 32.

The analysis for the 3^- state presented a technical problem: The values for $B(E3{:}0^+ \rightarrow 3^-)$ and the transition radius slowly increased with increasing cutoff radius R, whereas χ^2 decreased continuously. This problem is associated with the tail of the transition density at large radii r (see Fig. 11), which increased in amplitude as the cutoff radius was increased. In view of our findings for the other inelastic states in ^{192}Os, we chose 11 fm for the cutoff radius and accounted for the observed systematic increase in $B(E3)$ and R_{tr} by increasing the systematic error. The experimental results are given in Tables III and IV, and the cross sections are compared with the Fourier-Bessel fit in Fig. 10. The transition density of the 3^- state, like that of the 4^+ state, peaks somewhat inside the nuclear surface and also shows a significant negative lobe at about 3.5 fm. The gross features of the transition density, including the relatively large tail outside the nucleus, are similar to those observed[14] in the 3^- state at 5.345 MeV in ^{208}Pb. Since the octupole vibration in ^{192}Os is superimposed on a quadrupole deformation, we can anticipate that the originally degenerate 3^- state will be split into several states of different K, each with its separate rotational band. In the present experiment the $B(E3)$ value was determined to be 0.130 e^2b^3, i.e., about 8.5 W.u., which is very similar to the random-phase approximation (RPA) calculated strength of the 3^- band head (7.4 W.u.), as reported by Neegard and Vogel[33] for ^{190}Os. Since the RPA calculations suggest that the 3^- state strengths vary only slightly among the osmium isotopes, our observed strength in ^{192}Os seems to be entirely consistent with the RPA calculations.

5. *Higher states*

At some scattering angles, other excited states (see Fig. 1) rose above the radiation tail of the elastic peak and became visible in the spectrum. However, the carbon line obscured any such peaks below a momentum transfer of 1

TABLE VI. Comparison of the $B(E\lambda)$ values and transition radii for the $2^{+'}$ (489 keV) and 4^+ (580 keV) states of ^{192}Os with other experiments and calculations.

$B(E2{:}0^+ \rightarrow 2^{+'})$ (e^2b^2)	R_{tr} (fm)	Method	Ref.
0.189(32)	7.04(18)	(e,e')	This work
0.181(18)		Coul. exc.	47
0.2025		Coul. exc.	48
0.196(12)		Coul. exc.	50
0.184(27)		Coul. exc.	52
	6.94	HF (DME)	This work
0.177		IBA	31
0.150		IBA	34
0.035		PPQ	1
	6.83	Davydov+μ[a]	42
$B(E4{:}0^+ \rightarrow 4^+)$ (e^2b^4)	R_{tr} (fm)	Method	Ref.
0.0365(42)	6.894(83)	(e,e')	This work
0.343		Coul. exc.	48
0.0163		IBA	31
0.040		b	32
0.024	7.09	HF (DME)	This work

[a]Davydov transition density fitted to μ-atom data.
[b]Srutinsky method.

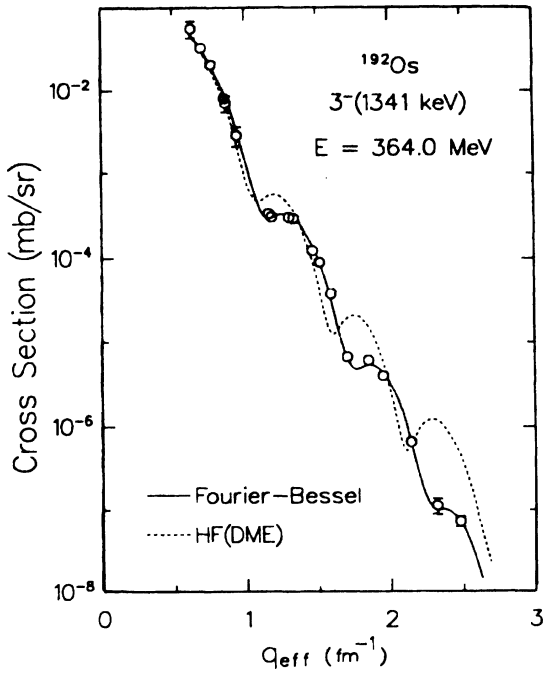

FIG. 10. Experimental inelastic electron-scattering cross sections (recalculated for 364 MeV) of the 3^- state (1341 keV) of ^{192}Os. The data are compared with the Fourier-Bessel fit and the Hartree-Fock calculation.

fm^{-1}. In general, our data for the higher states are sparse and have large uncertainties due to the radiation background of the elastic and lower lying inelastic states and to competition from target impurities. Therefore, analysis of these cross sections was not undertaken.

Of some interest, however, is the third 2^+ state in ^{192}Os, a member of the quasi β band, which has been predicted by the IBA (Ref. 34), BET (Ref. 35), and PPQ (Ref. 1) theories to lie at an excitation energy of 1.05, 0.93, and 1.12 MeV, respectively. This state is well known in the neighboring isotopes and occurs at 1.115 MeV in ^{190}Os and at 1.305 MeV in ^{188}Os. In a recent (n,n'γ) experiment,[36] a 2^+ state was observed at 1.127 MeV in ^{192}Os that decays dominantly to the 3^+ state of the γ band. However, for a member of the quasi β band we might expect decay mainly to the ground state band. In any case, the close proximity of the $2^{+''}$ state to the 4^+ state at 1.069 MeV and to the 6^+ ground state band member at 1.089 MeV makes it impossible with the present experimental resolution to uniquely distinguish any of these states.

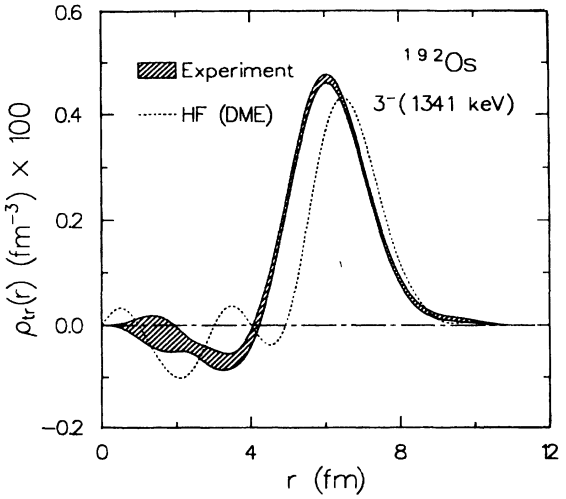

FIG. 11. Experimental transition charge density for the 3^- state (1341 keV) of ^{192}Os. The HF transition density is derived from the HF intrinsic density using the small-amplitude vibration expansion.

6. *Deformation parameters*

Intrinsic deformation parameters of a nucleus exist only within the context of a particular model. A common procedure for electron-scattering data is the method of fitting elastic and inelastic cross sections of the members of the ground state rotational band simultaneously to an intrinsic shape, given by a surface-deformed Fermi distribution. On the other hand, in the rotational model the β_λ parameters are directly related to the $B(E\lambda)$ values via a simple mathematical prescription. Using this procedure, the deformation parameters β_2 and β_4 were calculated from our experimental $B(E\lambda)$ values and found to be 0.15 and $(-)0.04$, respectively.

VI. COMPARISON WITH THEORY

A. Hartree-Fock theory

1. *Ground state*

Hartree-Fock (HF) theory probably represents the most thoroughly explored and successful theoretical method for microscopically describing the ground states of spherical and deformed nuclei. An HF study of the osmium and platinum nuclei, in which the Bardeen-Cooper-Schrieffer (BCS) pairing approximation was used and the self-consistent potential was derived from a Skyrme effective interaction, has been reported by Sauvage-Letessier *et al.*[37] However, the radial behavior of the density distribution is not presented in Ref. 37, and the calculated rms radius (see Table VII) exceeds our experimental result by 0.081 fm. We have therefore independently performed density-dependent HF calculations using the method of Vautherin[9] and Negele and Rinker.[10] The calculations assume axially symmetric nuclear deformation and use the density matrix expansion (DME) effective Hamiltonian and the pairing approximation described in Ref. 10. The DME method is appealing compared to the use of Skyrme forces, since it is based on a realistic two-body effective interaction rather than a purely phenomenological potential. The present work (and our previous Letter[11]) represent the first reported DME calculation for nuclei in the osmium-platinum region.

The HF calculations were performed using the code and procedure discussed in Ref. 10. If desired, the quadrupole moment can be constrained in the calculation, thus

TABLE VII. Comparison of the rms radius of ^{192}Os with the results of various Hartree-Fock calculations.

$\langle r^2\rangle^{1/2}$ (fm)	Method	Ref.
5.413(4)	(e,e′)+μ	This work
5.417	HF (DME)	This work
5.494[a]	HF + BCS	37
5.335[b]	HF (Skyrme)	53

[a]Deformed (prolate) solution.
[b]Spherical nucleus assumed.

making it possible to map out the energy of deformation versus quadrupole moment. The degree to which the predicted deformation of greatest binding energy matches the experimentally observed nuclear quadrupole deformation can be used to assess the validity of the calculation. The calculations were made using a basis consisting of 14 major harmonic oscillator shells. The pairing energy was obtained from experimental mass differences[38] between neighboring isotopes and isotones for each nucleus. The oscillator length and the basis deformation parameters were calculated from empirical relations obtained by adjusting the binding energy and internal density of ^{40}Ca. The HF calculations were performed on a Cray-1 computer, and each iteration required about 20 sec of CPU time. Typically 10—20 iterations were made at each of 10—15 quadrupole deformations to map out the binding energy versus deformation curve. At the minimum of the potential curve about 100 iterations were performed to guarantee convergence of the higher multipole orders.

We performed HF calculations for three nuclei in the transition region (^{188}Os, ^{192}Os, and ^{194}Pt) to investigate the ability of the method to predict the quadrupole deformation sign change that occurs in the osmium-platinum region. The binding energy versus deformation curves for ^{192}Os and ^{194}Pt are presented in Fig. 12. As we pointed out in Ref. 11, the experimental findings are rather well reproduced by HF theory: a prolate-oblate transition is predicted near ^{192}Os, and the intrinsic quadrupole moments, as defined by the deformation of greatest binding energy, are within a few percent of the values derived from experimental $B(E2{:}0^+\rightarrow 2^+)$ transition probabilities (see Table VIII). The predicted radial moments are also in remarkable agreement with the experimental values (Table VII).

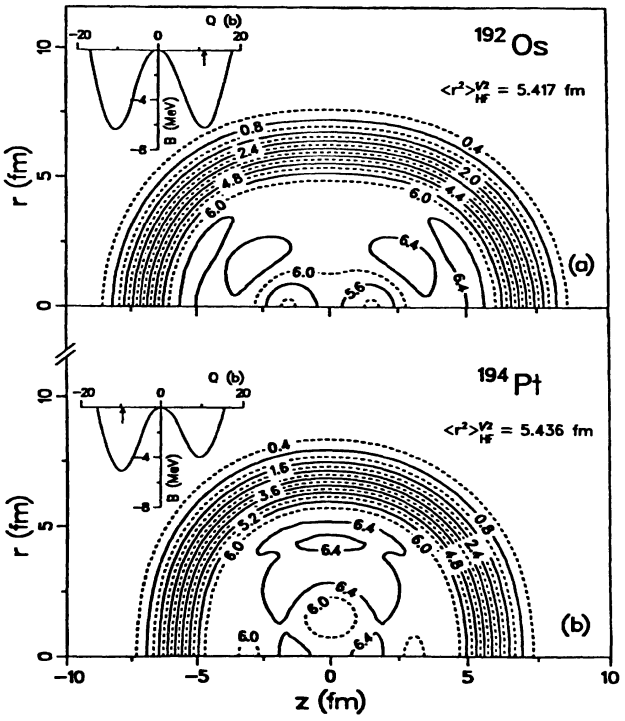

FIG. 12. Proton densities of ^{192}Os and ^{194}Pt computed by Hartree-Fock (DME) methods. The densities are (by assumption) symmetric about the z axis. The change from prolate to oblate shape is clearly evident. The computed binding energy versus intrinsic quadrupole mass deformation parameter Q for each nucleus is shown in the inserts. The arrows indicate the Q values computed from experimental $B(E2)$ values. The potential surface curve of ^{188}Os is very similar to that of ^{192}Os.

The computed ground-state charge density of ^{192}Os and that extracted from our experiment are compared in Fig. 3. The agreement is quite good: The small density oscillations at about one-half the nuclear radius are well reproduced in amplitude and position, and the predicted nuclear surface density is nearly indistinguishable from the experimental density. A comparison of these results in q space (Fig. 2) shows a visible deviation only for momentum transfers greater than 2.5 fm^{-1}.

TABLE VIII. Results of our Hartree-Fock calculations compared with experimental values.

Nucleus	Q_0 (e b) Expt.	Q_0 (e b) HF	rms radius (fm) Expt.	rms radius (fm) HF	R_k (fm) Expt.	R_k (fm) HF[b]	$(BE_{ex}-BE_{HF})/A$[a] (MeV)	ΔR_k (fm)
^{186}Os	568	615		5.409	6.8779(27)[c]	6.8923	0.069	−0.014
^{192}Os	448	434	5.413(3)[d]	5.417	6.9108(25)[c]	6.9088	0.052	0.002
^{194}Pt	403	374		5.436	6.9285(20)[e]	6.9312	0.045	−0.003

[a]Binding energies are taken from Ref. 38.
[b]The equivalent radii are calculated by using the HF (DME) monopole charge distribution and the values for k and α from Ref. 25.
[c]See Ref. 25.
[d]This work.
[e]Preliminary muonic atom results (unpublished).

2. Dynamics

In its present state, the HF theory discussed in the preceding section is able to represent only the intrinsic nuclear ground state; it makes no pretext at describing nuclear excitations. However, low-lying nuclear states in deformed nuclei can be described in terms of rotation and vibrations based on the intrinsic ground state. In this approximation, the ground state rotational band transition densities are obtained by Legendre expansion of the intrinsic density distribution as given by[10]

$$\rho_\lambda = \sqrt{(2\lambda+1)/4\pi} \int \rho_{\mathrm{HF}}(r,\Omega) Y^*_{\lambda 0}(\Omega) d\Omega \ . \tag{16}$$

In the model of small-amplitude vibrations, the members of the γ-vibrational band are related to the intrinsic ground state charge distribution by[39]

$$\rho^\gamma_\lambda(r) = \beta^\gamma \sqrt{2} \int Y^*_{\lambda 2}(\Omega) Y_{22}(\Omega) \frac{\delta\rho}{\delta r}(r,\Omega) d\Omega \ , \tag{17}$$

where the transition strength β^γ is adjusted (in the present analysis) to the experimental $B(e\lambda)$ value. Within the same model, one-phonon octupole vibrations are related to the intrinsic nuclear density[40] by

$$\rho^0_\lambda(r) = \gamma \int \frac{\delta\rho}{\delta r}(r,\Omega) Y_{\lambda 0}(\Omega) Y_{30}(\Omega) d\Omega + \xi \int Y_{\lambda 0}(\Omega) \frac{\delta\rho}{\delta r}(r,\Omega) d\Omega \ , \tag{18}$$

where γ and ξ are vibrational constants common to all states in the same band. The parameter ξ accounts for the center-of-mass correction in the presence of a pure isoscalar ($T=0$) transition. However, as discussed in Ref. 39, the center-of-mass correction can be neglected in first order (i.e., $\xi=0$), and we have therefore adjusted the single parameter γ to fit the observed $B(E3{:}0^+ \rightarrow 3^-)$ strength.

Figure 5 demonstrates that the transition density to the first 2^+ state is very well reproduced by the projection of the intrinsic HF charge density. The calculation follows the interior structure of the experimental density very well, despite neglect of possible triaxial or γ-soft character of ^{192}Os in the HF intrinsic state calculation. We should emphasize that the amplitude of the predicted transition density comes directly from projection of the intrinsic charge density—no renormalization using an effective charge is involved. The theoretical cross sections (Fig. 4) agree very well with the experimental data up to a momentum transfer of 2.5 fm^{-1}.

The 4^+ member of the ground-state rotational band is reasonably well described by the projected HF calculation as regards the shape of the transition density (Fig. 9), but the transition probability is about 35% underestimated. A similar situation has been observed in the case of the 4^+ state of ^{154}Gd (Ref. 17), while the nucleus ^{238}U (Ref. 39) shows reasonable agreement.

Using the experimental $B(E2)$ value from Table III for normalization, we derived the transition density of the second 2^+ state (γ vibration) from the intrinsic HF density via Eq. (17). The agreement with experiment (Fig. 7) is remarkably good; even the small density oscillations in the nuclear interior are qualitatively reproduced. The predicted cross sections (Fig. 6) show good agreement with experiment over the entire momentum transfer range for which we have data for this state.

The transition density for the 3^- level (1341 keV) was obtained from the intrinsic HF distribution by using Eq. (18) and the transition probability of Table III. The calculated shape of the transition density (Fig. 11), though surface peaked like the experimental density, has a transition radius that is clearly too large. The discrepancy in ^{192}Os is also evident when the experimental and theoretical cross sections are compared (Fig. 10). This deviation may indicate that the 3^- state is less collective than implied by a pure octupole vibrational representation. As pointed out in Ref. 33, the low-lying octupole states in the deformed region $152 \leq A \leq 190$ exhaust only a small part of the full octupole strength. The small-amplitude vibration model using the HF intrinsic density was found to be in good agreement with the experiment for the 3^- state (0.732 MeV) of the 0^- band in ^{238}U (Ref. 39). However, in the case of ^{238}U the $B(E3)$ value is considerably larger, amounting to about 25 W.u.

The HF calculations presented here were restricted to axial symmetry. The question arises as to what extent inclusion of nonaxial deformations would affect the predicted charge densities. This question is currently being investigated by Cartesian-coordinate-based HF calculations that contain no restrictions on deformation or nuclear symmetry.[41] Preliminary results reveal a calculated total binding energy that is astonishingly independent of the triaxial deformation parameter γ, which may be a factor in understanding the success of the present calculations that implicitly assume $\gamma=0$. No charge densities are yet available from these calculations.

B. Davydov model

Although the Davydov model[6] of a triaxially deformed rotor is based on somewhat unphysical assumptions, its equations of motion are similar to those of more realistic models[4] and, with appropriate parameter values, it is as capable as other existing models of describing the $E2$ transitions and low-energy excitation spectra of the Os nuclei. The model may be taken as representative of a class of collective macroscopic models and has the advantage of explicit inclusion of a variable γ related to axial symmetry.

We have normalized the Davydov transition densities for the 2^+ and $2^{+\prime}$ states of ^{192}Os, as presented in Ref. 42, to our experimental (e,e′) transition probabilities. A comparison with the electron-scattering results is shown in Figs. 5 and 7. The macroscopic basis of the Davydov model makes it incapable of predicting detailed structures in the nuclear interior, and the model therefore fails to describe the experimental form factors at higher momentum transfer. However, it exhibits reasonably good agreement at the nuclear surface for both the 2^+ and $2^{+\prime}$ states, and the calculated cross sections are of the same quality as the HF calculations up to a momentum transfer of 2 fm^{-1}.

C. IBA

Recently, a new approach to describing nuclear properties has been proposed, the interacting boson approxima-

tion (IBA) of Arima and Iachello.[7] In this model, the collective properties of nuclei are described in terms of pairs of nucleons coupled to angular momentum $L=0$ and 2, which are treated as bosons. The most general two-body Hamiltonian within the boson space is written in terms of the generators of the groups SU(6). It has been shown that in three special cases this Hamiltonian can be expressed in terms of generators of a subgroup of SU(6), namely the SU(5) group, the SU(3) group, and the O(6) group.[34]

In contrast to geometric models, in the IBA the states in each subgroup limit are associated into families according to their group representations. Thus, in SU(3) for example, the β and γ bands belong to the same representation but to a different one than does the ground-state band. On the other hand, in the O(6) limit the ground-state and γ band belong to the same representation.

Attempts to apply the IBA formalism to the density information available from electron scattering has so far had mixed success. In the simplest version (IBA-1), the collective $E2$ transition densities of the lowest 2^+ states of a nucleus should be linearly related to two basic boson charge densities $\alpha(r)$ and $\beta(r)$. This prediction seems to be reasonably well satisfied by electron scattering measurements on a sequence of samarium isotopes for the corresponding first 2^+ states,[52] but fails in ^{154}Gd (Ref. 43), where the three lowest 2^+ states of the same nucleus are considered. For the osmium isotopes, IBA-1 is known to be inadequate, and an approximation that distinguishes between neutron and proton bosons (IBA-2) is usually applied. Calculation of transition densities within the context of IBA-2 is more complex since a larger number of elementary boson densities is now involved. The influence of states outside the boson model space (core polarization) must also be considered. Scholten[44] has reported a microscopic IBA approach to the calculation of transition densities in transitional nuclei. Such calculations for ^{192}Os are currently in progress.[45,46]

VII. SUMMARY AND CONCLUSIONS

We have measured the elastic and inelastic electron scattering cross sections of ^{192}Os up to a momentum transfer of 2.9 fm^{-1}. The model-independent Fourier-Bessel method, in combination with muonic-atom data, has been used to determine the ground-state density and the transition densities for the 2^+, $2^{+\prime}$, 4^+, and 3^- states. These experimental results provide a body of charge-density distribution data against which present and future models of the dynamics of transitional nuclear models can be tested.

We have also reported the results of DME Hartree-Fock calculations for three transition-region nuclei: ^{188}Os, ^{192}Os, and ^{194}Pt. These calculations reproduce the charge radii and quadrupole deformation trends of the transitional nuclei unexpectedly well, and in particular the predicted ground-state density of ^{192}Os is in astonishingly good agreement with experiment. We have also approximated the low-lying excited-state transition densities of ^{192}Os by Legendre expansion of the HF-computed ground state and find these predictions to be in reasonable agreement with experiment.

We hope that the experimental data presented in this paper will encourage further attempts to understand transitional nuclei. In particular, continued work on nonaxially-constrained HF methods, together with exploration of HF calculations of excited states more realistic than the approximation present here, would appear to be fruitful. Hartree-Fock methods have historically been applied only to isolated nuclei because of the computing time required, but the increasing availability of fast virtual memory and Cray-class scientific computers promises to make the HF method a tool that can now be rather generally applied to gain a better understanding of nuclear structure and dynamics.

---

*Present address: Physics Department, University of Tübingen, Tübingen, Federal Republic of Germany.

[1]K. Kumar and M. Baranger, Phys. Rev. Lett. **17**, 1146 (1966); Nucl. Phys. **A92**, 608 (1967); **A122**, 273 (1968).
[2]U. Mosel and W. Greiner, Z. Phys. A **217**, 256 (1968).
[3]U. Gotz, H. C. Pauli, K. Alder, and K. Junker, Nucl. Phys. **A192**, 1 (1972).
[4]A. Faessler and W. Greiner, Z. Phys. **168**, 425 (1962); **170**, 105 (1962); **117**, 190 (1964).
[5]M. Girod and B. Grammaticos, Phys. Rev. Lett. **40**, 361 (1978).
[6]A. S. Davydov and G. Filippov, Nucl. Phys. **8**, 237 (1958).
[7]A. Arima and F. Iachello, Ann. Phys. (N.Y.) **99**, 253 (1976); **111**, 201 (1978); **123**, 468 (1979).
[8]T. Kishimoto and T. Tamura, Nucl. Phys. **A270**, 317 (1976).
[9]D. Vautherin, Phys. Rev. C **7**, 296 (1973).
[10]J. W. Negele and G. Rinker, Phys. Rev. C **15**, 1499 (1977).
[11]W. Reuter, E. B. Shera, M. V. Hoehn, F. W. Hersman, T. Milliman, J. M. Finn, C. Hyde-Wright, R. Lourie, B. Pugh, and W. Bertozzi, Phys. Lett. **137B**, 32 (1984).
[12]T. de Forest and J. D. Walecka, Adv. Phys. **15**, 1 (1966).
[13]J. Heisenberg, J. Lichtenstadt, C. N. Papanicolas, and J. S. McCarthy, Phys. Rev. C **25**, 2292 (1982).
[14]J. Heisenberg, Adv. Nucl. Phys. **12**, 61 (1981).
[15]W. Bertozzi, M. V. Hynes, C. P. Sargent, C. Creswell, P. C. Dunn, A. Hirsch, M. Leitch, B. Norum, F. N. Rad, and T. Sasanuma, Nucl. Instrum. Methods **141**, 457 (1977).
[16]W. Bertozzi, M. V. Hynes, C. P. Sargent, W. Turchinetz, and C. Williamson, Nucl. Instrum. Methods **162**, 211 (1979).
[17]F. W. Hersman, Ph.D. thesis, MIT, 1982; Phys. Rev. C (to be published).
[18]W. Reuter, J. C. Gursky, E. B. Shera, and M. W. Johnson, Nucl. Instrum. Methods **220**, 288 (1984).
[19]J. Bergstrom, in Medium Energy Nuclear Physics, MIT Report TID-24667, 1967, edited by W. Bertozzi and S. Kowalski.

[20]W. Reuter, G. Fricke, K. Merle, and H. Miska, Phys. Rev. C **26**, 806 (1982).
[21]B. E. Norum, M. V. Hynes, H. Miska, W. Bertozzi, J. Kelly, S. Kowalski, F. N. Rad, C. P. Sargent, T. Sasanuma, W. Turchinetz, and B. L. Berman, Phys. Rev. C **25**, 1778 (1982).
[22]B. Dreher, J. Friedrich, K. Merle, H. Rothhaas, and G. Luhrs, Nucl. Phys. **A235**, 219 (1974).
[23]R. Barrett, Phys. Lett. **33B**, 388 (1970).
[24]H. D. Wohlfahrt, O. Schwentker, G. Fricke, H. G. Andersen, and E. B. Shera, Phys. Rev. C **22**, 264 (1980).
[25]M. V. Hoehn, E. B. Shera, H. D. Wohlfahrt, Y. Yamazaki, R. M. Steffen, and R. K. Sheline, Phys. Rev. C **24**, 1667 (1981).
[26]H. D. Wohlfahrt, Habilitationsschrift, University of Mainz, 1976 (unpublished).
[27]W. Reuter, E. B. Shera, H. D. Wohlfahrt, and Y. Tanaka, Phys. Lett. **124B**, 293 (1983).
[28]J. Heisenberg, Computer program HEINEL (unpublished).
[29]M. A. Moinester, J. Alster, G. Azuelos, J. B. Bellicard, B. Frois, M. Huet, P. Leconte, and Phan Xuan Ho, Phys. Rev. C **24**, 80 (1981).
[30]R. Hofmann, thesis KPH 29/80, University of Mainz, 1980.
[31]F. T. Baker, M. A. Grimm, Jr., A. Scott, R. C. Styles, T. H. Kruse, K. Jones, and R. Suchannek, Nucl. Phys. **A371**, 68 (1981).
[32]B. Nerlo-Pomarska, Nucl. Phys. **A259**, 481 (1976).
[33]K. Neergard and P. Vogel, Nucl. Phys. **A145**, 33 (1970).
[34]R. Bijker, A. E. L. Dieperink, O. Scholten, and R. Spanhoff, Nucl. Phys. **A344**, 207 (1980).
[35]K. J. Weeks and T. Tamura, Phys. Rev. C **22**, 1323 (1980).
[36]E. W. Kleppinger and S. W. Yates, Phys. Rev. C **27**, 2608 (1983).
[37]J. Sauvage-Letessier, P. Quentin, and H. Flocard, Nucl. Phys. **A370**, 231 (1981).
[38]A. H. Wapstra and K. Bos, At. Data Nucl. Data Tables **19**, 185 (1977).
[39]C. W. Creswell, Ph.D. thesis, MIT, 1977.
[40]A. Hirsch, C. Creswell, W. Bertozzi, J. Heisenberg, M. V. Hynes, S. Kowalski, H. Miska, B. Norum, F. N. Rad, C. P. Sargent, T. Sasanuma, and W. Turchinetz, Phys. Rev. Lett. **40**, 632 (1978).
[41]H. Flocard (private communication).
[42]Y. Tanaka and R. M. Steffen, Nucl. Phys. **A382**, 513 (1982).
[43]F. W. Hersman, W. Bertozzi, T. N. Buti, J. M. Finn, C. Hyde-Wright, M. V. Hynes, J. Kelly, M. A. Kovash, S. Kowalski, J. Lichtenstadt, R. Lourie, B. Murdock, B. Pugh, F. N. Rad, C. P. Sargent, and J. B. Bellicard, Phys. Lett. **132B**, 47 (1983).
[44]O. Scholten, Bull. Am. Phys. Soc. **28**, 662, (1983).
[45]O. Scholten (private communication).
[46]G. Ginnochio (private communication).
[47]D. Cline *et al.* (private communication).
[48]F. T. Baker, T. H. Kruse, W. Hartwig, I. Y. Lee, and J. X. Saladin, Nucl. Phys. **A258**, 43 (1976).
[49]S. A. Lane and J. X. Saladine, Phys. Rev. C **6**, 613 (1972).
[50]W. T. Milner, F. K. McGowan, R. L. Robinson, P. H. Stelson, and R. O. Sayer, Nucl. Phys. **A177**, 1 (1971).
[51]R. J. Pryor and J. X. Saladin, Phys. Rev. C **1**, 1573 (1970).
[52]R. F. Casten, J. S. Greenberg, G. A. Burginyon, and D. A. Bromley, Phys. Rev. Lett. **18**, 912 (1967).
[53]J. Friedrich, P. G. Reinhard, and N. Voegler (unpublished).